Robotica (2019) volume 37, pp. 1073–1089. © Cambridge University Press 2019
doi:10.1017/S0263574718001443

A Feedback Linearization-Based Motion Controller for a UWMR with Experimental Evaluations

Luis Montoya-Villegas†*, Javier Moreno-Valenzuela† and Ricardo Pérez-Alcocer‡

†*Instituto Politécnico Nacional-CITEDI, Av. Instituto Politécnico Nacional No. 1310, Colonia Nueva Tijuana, Tijuana, Baja California 22435, México*
E-mail: moreno@citedi.mx
‡*CONACYT-Instituto Politécnico Nacional-CITEDI, Av. Instituto Politécnico Nacional No. 1310, Colonia Nueva Tijuana, Tijuana, Baja California 22435, México*
E-mail: rrperez@citedi.mx

(Accepted December 12, 2018. First published online: January 18, 2019)

SUMMARY
In this paper, the feedback linearization approach is used to introduce a motion controller for unicycle-type wheeled mobile robots (UWMRs). The output function is defined as a linear combination of the error state. The novel scheme is firstly tested in numerical simulation and compared with its corresponding experimental result. Three controllers are taken from the literature and compared to the proposed approach by means of experiments. The gains of the experimentally tested controllers are selected to obtain identical energy consumption. The Optitrack commercial vision system and Pioneer P3-DX UWMR are used in real-time experimental tests. In addition, two sets of experimental results for different motion tasks are provided. The results show that the proposed controller presents the best tracking accuracy.

KEYWORDS: Trajectory tracking; Mobile robots; Feedback linearization; Vision system; Real-time experiments.

1. Introduction

Underactuated systems have been studied for several years.[1,2] These types of systems have more degrees of freedom than actuators. The design of control schemes is a complex task for unicycle-type wheeled mobile robots (UWMRs) because of the movement restrictions and model complexity. Recent advances in the control of underactuated systems include cascade control strategies for an inertial wheel pendulum,[3] control H_∞ in the presence of disturbances for vehicles of two balanced wheels[4] and satellites,[5] robust control backstepping to control a quadrotor,[6] a proportional-integral-derivative controller with a sliding mode scheme for unmanned aquatic robots,[7] and a sliding mode controller for autonomous aquatic robots.[8]

Mobile robotics has prompted the interest of the scientific community in recent years. UWMRs have attracted more attention due to their simplicity and good mobility. Thus, much effort has been devoted to overcoming the limitations of the reported control algorithms to reduce the error levels in trajectory tracking or position regulation. In ref. [9], two models for UWMRs were presented. These models consider a displacement of the body reference frame with respect to the axis of

* Corresponding author. E-mail: lmontoya@citedi.mx

https://doi.org/10.1017/S0263574718001443 Published online by Cambridge University Press

the wheels. One model considers the linear and angular velocities as the input signal, and the other uses the angular velocities of the wheels as the control action. In ref. [10], position control was performed using a kinematic model in polar coordinates, where adaptive control was proposed to compensate for the unknown model parameters. The results were validated in numerical simulation and real-time experiments with the Pioneer 3-DX mobile robot. A controller based on Lyapunov's theory was proposed in ref. [11], which was used for both regulation and trajectory tracking. This controller was validated in numerical simulation and real-time experiments using a Pioneer 2-DX mobile robot. In ref. [12], a servo-controller was proposed for trajectory tracking of UWMRs with bounded speed and torque. The results were validated in a numerical simulation and real-time experiments using a Pioneer 3-DX mobile robot. In ref. [13], a performance comparison of two trajectory tracking controllers was presented using the kinematic model of a UWMR: one based on Lyapunov's techniques and the other developed using linear algebra methods. In ref. [14], a kinematic level adaptive controller was proposed for a UWMR with longitudinal slippage. In this work, the authors assumed that the desired velocity and its derivatives were bounded. In ref. [15], two control techniques were proposed to track the trajectories of UWMRs using a modified kinematic model of four states: one technique was developed based on the fuzzy Takagi–Sugeno model with parallel distributed compensation control, and the other was designed using Lyapunov's stability theory. The performance of both controllers was compared in numerical simulation.

Although different techniques were used by the authors of the above-cited works, various methods to generate control schemes continue to be studied and applied. The controllers designed by Lyapunov's direct method and backstepping technique are the most common techniques. A method that was not recently developed but has also aroused interest in the scientific community is feedback linearization control, as it has the advantage of mathematically transforming a nonlinear dynamic system into a linear one; hence, linear control techniques can be applied. Current applications of this technique are as follows. In ref. [16], a control algorithm based on linearization by the output feedback was proposed to control a mobile robot with two manipulator arms. A numerical simulation was performed for controller verification. In ref. [17], two platforms were combined: a mobile robot with wheels and a parallel robot driven by a cable to obtain the combined kinematic and dynamics equations. These equations were linearized by the output feedback to obtain the controller, which was validated in a numerical simulation and real-time experiments. In ref. [18], a new adaptive controller was designed via sliding modes for heavy deliveries by parachute from an airship, where the controller was designed with feedback linearization techniques. The controller was analyzed by Lyapunov's stability theory, and validation was performed by numerical simulation. In ref. [19], decentralized training control was presented for a set of quadrotors using output feedback linearization techniques. Comparisons of numerical simulation results were provided.

The previous literature review shows that the application of the feedback linearization control technique in UWMRs requires a deeper understanding, which this paper aims to contribute to.

The contributions of this document are summarized as follows. The design of a new controller for UWMRs based on the technique of output feedback linearization for trajectory tracking is introduced. The novel scheme is firstly tested in numerical simulation and compared with its corresponding experiment result. Supported by real-time experiments, the performance of the new controller is analyzed and compared with three controllers in the literature[20–22] based on the energy demanded by the controllers. In other words, the gains of the tested controllers, including the proposed one, are selected to obtain identical energy consumption in experiment. In particular, the real-time implementations are performed with the Pioneer P3-DX robot and Optitrack vision system.

This paper is organized as follows: In Section 2, the kinematic model of the UWMR is presented, the control problem is formulated, and the open-loop dynamics is discussed. In Section 3, a new control law based on feedback linearization and the stability analysis for the overall closed-loop system are provided. Simulation results for the proposed controller, the experimental platform, and experimental comparison results for circular and lemniscate paths are described in Section 4. Finally, conclusions are provided in Section 5.

https://doi.org/10.1017/S0263574718001443 Published online by Cambridge University Press

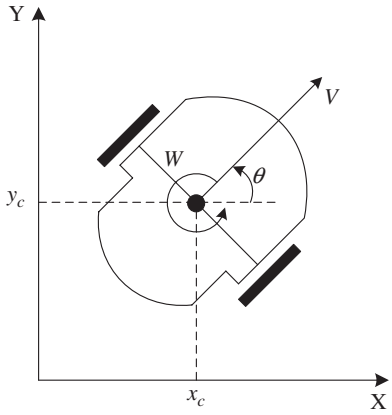


Fig. 1. Diagram of the UWMR.

2. Unicycle Mobile Robot

In this section, the model of the UWMR is introduced. The tracking errors are defined, and the control problem is expressed.

2.1. Kinematic model

The kinematic model of the UWMR is

$$\dot{x_c} = V\cos(\theta), \tag{1}$$
$$\dot{y_c} = V\sin(\theta), \tag{2}$$
$$\dot{\theta} = W, \tag{3}$$

where x_c and y_c are the coordinates of the centre of mass of the vehicle (position of the midpoint of the axis that joins the wheels), θ is the orientation of the vehicle, V is the forward linear velocity, and W is the angular velocity. Figure 1 shows a scheme of the UWMR.

The vehicle kinematics satisfies the equation

$$\dot{x_c}\sin(\theta) - \dot{y_c}\cos(\theta) = 0, \tag{4}$$

which is a nonholonomic constraint.[23]

The mobile robot in the kinematic model (1)–(3) denotes a three-degree-of-freedom system with two control inputs (forward velocity and angular velocity).[23] Thus, the mobile robot is an underactuated system because the external generalized inputs $[V\ W]^T$ cannot command instantaneous velocities in all directions in the configuration space.

2.2. Control problem formulation

In this work, the trajectory tracking problem is considered. The virtual reference UWMR is given by

$$\dot{x}_r = V_r\cos(\theta_r), \tag{5}$$
$$\dot{y}_r = V_r\sin(\theta_r), \tag{6}$$
$$\dot{\theta}_r = W_r, \tag{7}$$

where the subscript r stands for reference. Signals V_r, W_r, $\dot{V}_r$, $\dot{W}_r \in \mathbb{R}$ are assumed to be bounded.

Thus, the control problem is to find a feedback control law $[V\ W]^T \in \mathbb{R}^2$ such that the limit

$$\lim_{t\to\infty} \begin{bmatrix} x_r(t) \\ y_r(t) \\ \theta_r(t) \end{bmatrix} - \begin{bmatrix} x_c(t) \\ y_c(t) \\ \theta(t) \end{bmatrix} = \begin{bmatrix} 0 \\ 0 \\ 0 \end{bmatrix} \tag{8}$$

is satisfied.

https://doi.org/10.1017/S0263574718001443 Published online by Cambridge University Press

Let us notice that any path $(x_r(t),\ y_r(t))$ with bounded first- and second-time derivatives satisfies the Eqs. (5)–(7) if the reference orientation is given by

$$\theta_r(t) = \text{atan2}(\dot{y}_r(t), \dot{x}_r(t)), \tag{9}$$

where atan2(y, x) denotes the two-argument arctangent function returning the angle between the positive x-axis of a plane and the point $(x,\ y)$ on it. The reference angle $\theta_r(t)$ satisfies Eq. (4). Besides, the reference linear velocity V_r computed from Eqs.(5)–(7) as the norm of $\left[\dot{x}_r\ \dot{y}_r\right]^T$ is given by

$$V_r = \sqrt{\dot{x}_r^2 + \dot{y}_r^2}, \tag{10}$$

and the reference angular velocity W_r is obtained by differentiating Eq. (9) with respect to the time, that is,

$$W_r = \dot{\theta}_r = \frac{\dot{x}_r \ddot{y}_r - \ddot{x}_r \dot{y}_r}{\dot{x}_r^2 + \dot{y}_r^2}. \tag{11}$$

See further discussions on the motion planning for UWMRs in refs. [24] and [25].

2.3. Open-loop error dynamics

The tracking error is defined as

$$\begin{bmatrix} \tilde{x} \\ \tilde{y} \\ \tilde{\theta} \end{bmatrix} = \begin{bmatrix} x_r - x_c \\ y_r - y_c \\ \theta_r - \theta \end{bmatrix}. \tag{12}$$

Nevertheless, a common approach in tracking control design is to apply a coordinate change as follows:[20,26]

$$\begin{bmatrix} e_1 \\ e_2 \\ e_3 \end{bmatrix} = \begin{bmatrix} \cos(\theta) & \sin(\theta) & 0 \\ -\sin(\theta) & \cos(\theta) & 0 \\ 0 & 0 & 1 \end{bmatrix} \begin{bmatrix} \tilde{x} \\ \tilde{y} \\ \tilde{\theta} \end{bmatrix}, \tag{13}$$

where e_l and e_2 are related to the position error signals, and e_3 is equal to the orientation error.

Differentiating Eq. (13) and substituting Eqs. (1)–(3) and Eqs. (5)–(7), we obtain the open-loop error dynamics

$$\frac{d}{dt}\begin{bmatrix} e_1 \\ e_2 \\ e_3 \end{bmatrix} = \begin{bmatrix} -V + We_2 + V_r \cos(e_3) \\ -We_1 + V_r \sin(e_3) \\ W_r - W \end{bmatrix}. \tag{14}$$

3. Proposed Controller Based on Feedback Linearization

To introduce a new feedback linearization controller, the open-loop error dynamics (14) can be rewritten in the following form:

$$\frac{d}{dt}\boldsymbol{e} = \underbrace{\begin{bmatrix} V_r \cos(e_3) \\ V_r \sin(e_3) - We_1 \\ W_r \end{bmatrix}}_{\boldsymbol{f}} + \underbrace{\begin{bmatrix} -1 & e_2 \\ 0 & 0 \\ 0 & -1 \end{bmatrix}}_{G} \begin{bmatrix} V \\ W \end{bmatrix}, \tag{15}$$

which is structured as

$$\frac{d}{dt}\boldsymbol{e} = \boldsymbol{f}(t, \boldsymbol{e}) + G(\boldsymbol{e})\boldsymbol{u},$$

where $\boldsymbol{e} \in \mathbb{R}^3$ is the state, $G \in \mathbb{R}^{3\times 2}$ is the input matrix, and $\boldsymbol{u} = [V\ W]^T \in \mathbb{R}^2$ is the control input.

https://doi.org/10.1017/S0263574718001443 Published online by Cambridge University Press

Let us define the time-varying vectors

$$\boldsymbol{k}_\alpha(t) = \begin{bmatrix} \alpha_1(t) \\ \alpha_2(t) \\ \alpha_3(t) \end{bmatrix}$$

and

$$\boldsymbol{k}_\beta(t) = \begin{bmatrix} \beta_1(t) \\ \beta_2(t) \\ \beta_3(t) \end{bmatrix}.$$

Inspired by ref. [1], we introduce the following output function:

$$\boldsymbol{y} = \begin{bmatrix} y_1 \\ y_2 \end{bmatrix} = \begin{bmatrix} \boldsymbol{k}_\alpha(t)^T \boldsymbol{e} \\ \boldsymbol{k}_\beta(t)^T \boldsymbol{e} \end{bmatrix} = \begin{bmatrix} \alpha_1(t)e_1 + \alpha_2(t)e_2 + \alpha_3(t)e_3 \\ \beta_1(t)e_1 + \beta_2(t)e_2 + \beta_3(t)e_3 \end{bmatrix}, \tag{16}$$

which corresponds to a linear combination of the error state. In this case, we have assumed that the error e_i is weighted by a time-varying signal $\alpha_i(t)$ or $\beta_i(t)$, which is conveniently selected as later shown. Since the input $\boldsymbol{u}$ has dimension two, the designed output $\boldsymbol{y}$ should be a two-dimensional signal, which is motivated by the theory of feedback linearization control established in ref. [28, p. 262.]

The vectors $\boldsymbol{k}_\alpha(t)$ and $\boldsymbol{k}_\beta(t)$ are designed as time-varying functions with first-time derivatives. Their components have been selected to obtain a well-defined control input $\boldsymbol{u}$ and to shape the stability of the internal dynamics as follows.

The time derivative of the output function $\boldsymbol{y}$ in Eq. (16) is computed as follows:

$$\begin{aligned} \dot{\boldsymbol{y}} &= \begin{bmatrix} \dot{y}_1 \\ \dot{y}_2 \end{bmatrix} = \begin{bmatrix} \alpha_1(t)\dot{e}_1 + \alpha_2(t)\dot{e}_2 + \alpha_3(t)\dot{e}_3 \\ \beta_1(t)\dot{e}_1 + \beta_2(t)\dot{e}_2 + \beta_3(t)\dot{e}_3 \end{bmatrix} + \begin{bmatrix} \dot{\alpha}_1(t)e_1 + \dot{\alpha}_2(t)e_2 + \dot{\alpha}_3(t)e_3 \\ \dot{\beta}_1(t)e_1 + \dot{\beta}_2(t)e_2 + \dot{\beta}_3(t)e_3 \end{bmatrix} \\ &= \begin{bmatrix} \boldsymbol{k}_\alpha^T \boldsymbol{f} \\ \boldsymbol{k}_\beta^T \boldsymbol{f} \end{bmatrix} + \begin{bmatrix} \boldsymbol{k}_\alpha^T G\boldsymbol{u} \\ \boldsymbol{k}_\beta^T G\boldsymbol{u} \end{bmatrix} + \begin{bmatrix} \dot{\boldsymbol{k}}_\alpha^T \boldsymbol{e} \\ \dot{\boldsymbol{k}}_\beta^T \boldsymbol{e} \end{bmatrix}, \end{aligned} \tag{17}$$

where the dependence on time of signals $\boldsymbol{k}_\alpha(t)$, $\boldsymbol{k}_\beta(t)$, $\dot{\boldsymbol{k}}_\alpha(t)$, and $\dot{\boldsymbol{k}}_\beta(t)$ has been omitted in the last expression.

The multi-input multi-output system in Eqs. (15)–(16) has a relative degree of 1 since, after differentiating $\boldsymbol{y}$ with respect to time, the control input $\boldsymbol{u}$ appears, and the output function $\boldsymbol{y}$ has dimension 2.

By expanding the second term of Eq. (17), we obtain

$$\dot{\boldsymbol{y}} = \begin{bmatrix} \boldsymbol{k}_\alpha^T \boldsymbol{f} \\ \boldsymbol{k}_\beta^T \boldsymbol{f} \end{bmatrix} + E(t, \boldsymbol{e}) \begin{bmatrix} V \\ W \end{bmatrix} + \begin{bmatrix} \dot{\boldsymbol{k}}_\alpha^T \boldsymbol{e} \\ \dot{\boldsymbol{k}}_\beta^T \boldsymbol{e} \end{bmatrix}, \tag{18}$$

where

$$E(t, \boldsymbol{e}) = \begin{bmatrix} -\alpha_1(t) & \alpha_1(t)e_2 - \alpha_3(t) \\ -\beta_1(t) & \beta_1(t)e_2 - \beta_3(t) \end{bmatrix}. \tag{19}$$

Finally, the following control input can be synthesized:

$$\begin{bmatrix} V \\ W \end{bmatrix} = E(t, \boldsymbol{e})^{-1} \left[- \begin{bmatrix} \boldsymbol{k}_\alpha^T \boldsymbol{f} \\ \boldsymbol{k}_\beta^T \boldsymbol{f} \end{bmatrix} - \begin{bmatrix} \dot{\boldsymbol{k}}_\alpha^T \boldsymbol{e} \\ \dot{\boldsymbol{k}}_\beta^T \boldsymbol{e} \end{bmatrix} - K_p \boldsymbol{y} \right], \tag{20}$$

where $K_p \in \mathbb{R}^{2\times 2}$.

https://doi.org/10.1017/S0263574718001443 Published online by Cambridge University Press

By substituting Eq. (20) into system (18), we obtain

$$\frac{d}{dt}\begin{bmatrix} y_1 \\ y_2 \end{bmatrix} = -K_p \begin{bmatrix} y_1 \\ y_2 \end{bmatrix},$$

which is an exponentially stable system if $K_p = K_p^T > 0$.

An important observation is that matrix $E(t, \boldsymbol{e})$ in Eq. (19), which is related to the control input (20), can be turned into a globally invertible matrix. In other words,

$$E(t, \boldsymbol{e})^{-1} = \frac{1}{\alpha_1(t)\beta_3(t) - \beta_1(t)\alpha_3(t)} \begin{bmatrix} \beta_1(t)e_2 - \beta_3(t) & -\alpha_1(t)e_2 + \alpha_3(t) \\ \beta_1(t) & -\alpha_1(t) \end{bmatrix}$$

exists if the gains $\alpha_i(t)$ and $\beta_i(t)$ satisfy

$$\det(E) = \alpha_1(t)\beta_3(t) - \beta_1(t)\alpha_3(t) \neq 0. \tag{21}$$

In an explicit form, omitting the time dependence of α_i and β_i, taking into account that $\boldsymbol{f} = [f_1 \;\; f_2 \;\; f_3]^T \in \mathbb{R}^3$ is a vector, whose components are defined in Eq. (15), and considering that $K_p = diag\{k_{p1}, \; k_{p2}\}$ is positive definite, the control input (20) can be explicitly given as

$$\begin{aligned} V = \frac{1}{\det(E)} \big[& (\beta_1 e_2 - \beta_3)(-\alpha_1 f_1 - \alpha_2 f_2 - \alpha_3 f_3 - \dot{\alpha}_1 e_1 - \dot{\alpha}_2 e_2 - \dot{\alpha}_3 e_3 - k_{p1} y_1) \\ & + (-\alpha_1 e_2 + \alpha_3)(-\beta_1 f_1 - \beta_2 f_2 - \beta_3 f_3 - \dot{\beta}_1 e_1 - \dot{\beta}_2 e_2 - \dot{\beta}_3 e_3 - k_{p2} y_2) \big] \end{aligned}$$

and

$$\begin{aligned} W = \frac{1}{\det(E)} \big[& \beta_1(-\alpha_1 f_1 - \alpha_2 f_2 - \alpha_3 f_3 - \dot{\alpha}_1 e_1 - \dot{\alpha}_2 e_2 - \dot{\alpha}_3 e_3 - k_{p1} y_1) \\ & - \alpha_1(-\beta_1 f_1 - \beta_2 f_2 - \beta_3 f_3 - \dot{\beta}_1 e_1 - \dot{\beta}_2 e_2 - \dot{\beta}_3 e_3 - k_{p2} y_2) \big]. \end{aligned} \tag{22}$$

Note that in expression (22), the angular velocity W appears on both sides of the equation since f_2 depends on W. To avoid the implicit representation, we select the gains such that

$$-\beta_1\alpha_2 + \alpha_1\beta_2 = 0. \tag{23}$$

Using some algebra, we obtain

$$\begin{aligned} W = \frac{1}{\det(E)} \big[& \beta_1(-\alpha_3 f_3 - \dot{\alpha}_1 e_1 - \dot{\alpha}_2 e_2 - \dot{\alpha}_3 e_3 - k_{p1} y_1) \\ & -\alpha_1(-\beta_3 f_3 - \dot{\beta}_1 e_1 - \dot{\beta}_2 e_2 - \dot{\beta}_3 e_3 - k_{p2} y_2) \big]. \end{aligned}$$

Then, to simplify the coming analysis, it is convenient to define more constraints in the gains α_i and β_i related to the output function $\boldsymbol{y}$ in Eq. (16). Specifically, we will consider that

$$\alpha_1, \, \beta_1, \, \beta_3 > 0, \tag{24}$$

$\alpha_2(t)$ is a time-varying differentiable signal,

$$\alpha_3 = 0, \tag{25}$$

and, according to condition (23),

$$\beta_2(t) = \alpha_2(t)\frac{\beta_1}{\alpha_1}, \tag{26}$$

so

$$\boldsymbol{k}_\alpha(t) = \begin{bmatrix} \alpha_1 \\ \alpha_2(t) \\ 0 \end{bmatrix}, \; \boldsymbol{k}_\beta(t) = \begin{bmatrix} \beta_1 \\ \beta_2(t) \\ \beta_3 \end{bmatrix} = \begin{bmatrix} \beta_1 \\ \alpha_2(t)\beta_1/\alpha_1 \\ \beta_3 \end{bmatrix}. \tag{27}$$

https://doi.org/10.1017/S0263574718001443 Published online by Cambridge University Press

Under conditions (24)–(27), the control inputs V and W become

$$V = \frac{1}{\det(E)}\left[(\beta_1 e_2 - \beta_3)(-\alpha_1 f_1 - \alpha_2 f_2 - \dot{\alpha}_2 e_2 - k_{p1} y_1) \right. \\ \left. -\alpha_1 e_2(-\beta_1 f_1 - \beta_2 f_2 - \beta_3 f_3 - \dot{\beta}_2 e_2 - k_{p2} y_2)\right] \tag{28}$$

and

$$W = \frac{1}{\det(E)}\left[\beta_1(-\alpha_3 f_3 - \dot{\alpha}_2 e_2 - k_{p1} y_1) - \alpha_1(-\beta_3 f_3 - \dot{\beta}_2 e_2 - k_{p2} y_2)\right], \tag{29}$$

where f_1, f_2, and f_3 are the components of vector $\boldsymbol{f}$ in Eq. (15).

It is worth noting that $f_2 = V_r \sin(e_3) - We_1$, where in the computer-based implementation, the angular velocity W should be first computed. Then, the signal f_2 and linear velocity V can be defined.

By following the output feedback linearization framework,[1,27,28] let us consider the following change of coordinates:

$$\boldsymbol{z} = \begin{bmatrix} \eta \\ y_1 \\ y_2 \end{bmatrix}, \tag{30}$$

where η satisfies

$$\frac{\partial \eta}{\partial \boldsymbol{e}} G(t, \boldsymbol{e}) = 0. \tag{31}$$

By proposing $\eta = e_2$, Eq. (31) can also be written as

$$\frac{\partial \eta}{\partial \boldsymbol{e}} G(t, \boldsymbol{e}) = \begin{bmatrix} 0 & 1 & 0 \end{bmatrix} \begin{bmatrix} -1 & e_2 \\ 0 & 0 \\ 0 & -1 \end{bmatrix} = \begin{bmatrix} 0 & 0 \\ 0 & 0 \\ 0 & 0 \end{bmatrix}.$$

Then, the change in coordinates (30) can be written as

$$\boldsymbol{z} = \begin{bmatrix} \eta \\ y_1 \\ y_2 \end{bmatrix} = \underbrace{\begin{bmatrix} 0 & 1 & 0 \\ \alpha_1 & \alpha_2 & 0 \\ \beta_1 & \beta_2 & \beta_3 \end{bmatrix}}_{H} \begin{bmatrix} e_1 \\ e_2 \\ e_3 \end{bmatrix}, \tag{32}$$

where condition (23) was considered. The inverse of H exists if Eq. (21) is satisfied.

It is worth noticing that the open loop system (15) could have been written with different parameterization for $\boldsymbol{f}$ and G. Specifically, the input term We_1 could have been included into the term $G \begin{bmatrix} V \\ W \end{bmatrix}$. However, the condition (31) becomes a system of coupled partial differential equations that is difficult to be solved. In others words the representation in Eq. (15) makes easier the obtention of the internal dynamics.

Using Eq. (32), its inverse and definition (21), the internal dynamics can be computed as follows:

$$\begin{aligned} \frac{d}{dt}\eta = \dot{e}_2 &= -We_1 + V_r \sin(e_3) \\ &= -\frac{\left[\det(E)\, W_r - \beta_1 k_{p1} y_1 + \alpha_1 k_{p2} y_2\right]}{\det(E)^2}\left[-(\alpha_2 \beta_3)\,\eta + \beta_3 y_1\right] \\ &\quad + V_r \sin\left(\frac{1}{\alpha_1 \beta_3}\left[-\beta_1 y_1 + \alpha_1 y_2\right]\right), \end{aligned} \tag{33}$$

https://doi.org/10.1017/S0263574718001443 Published online by Cambridge University Press

and the external dynamics is expressed here for reference:

$$\frac{d}{dy}\boldsymbol{y} = -K_p \boldsymbol{y}. \tag{34}$$

Eqs. (33) and (34) can be considered the overall closed-loop system.

Proposition 1. *If conditions* (24), (25), *and* (26) *are satisfied and we select*

$$\alpha_2(t) = -k_0 W_r(t), \tag{35}$$

with $W_r(t)$ *as a persistently exciting signal, the equilibrium* $\boldsymbol{z} = 0$ *of the overall closed-loop system* (33)–(34) *is locally asymptotically stable.*

Proof. By assuming $\boldsymbol{y} = 0$ in the internal dynamics (33), the zero dynamics can be written as

$$\frac{d}{dt}\eta = \frac{W_r}{\det(E)}\alpha_2\beta_3\eta = W_r\frac{\alpha_2}{\alpha_1}\eta. \tag{36}$$

The system (36) represents the internal dynamics unperturbed by the external dynamics (34). If we select $\alpha_2(t)$ as in condition (35), then

$$\frac{d}{dt}\eta = -k_0\frac{W_r^2(t)}{\alpha_1}\eta. \tag{37}$$

If $W_r(t)$ is persistently exciting, $\eta(t) \to 0$ as $t \to \infty$ with an exponential convergence rate; see Theorem 2.5.1 in ref. [29, p. 73]. On the other hand, the external dynamics (34) is an exponentially stable state.

The overall closed-loop system (33)–(34) has a cascade system structure, in which the unperturbed system (33) is asymptotically stable (see Eq. (37)) and the independent system (34) is exponentially stable. Thus, there are sufficient conditions to prove that the state space origin of Eqs. (33)–(34) is locally asymptotically stable; see ref. [30]. □

Proposition 2. *Because the solutions* $\boldsymbol{z}(t) = [\eta(t)\ \boldsymbol{y}(t)]^T \in \mathbb{R}^3$ *asymptotically converge to zero, the solutions of the error dynamics* $\boldsymbol{e}(t) = [e_1(t)\ e_2(t)\ e_3(t)]^T \in \mathbb{R}^3$ *also asymptotically converge to zero.*

Proof. Because $\boldsymbol{e}(t) = H^{-1}\boldsymbol{z}(t)$, the upper bound of the state vector $\boldsymbol{e}(t)$ can be expressed as $\| \boldsymbol{e}(t) \| \leq \| H^{-1} \| \| \boldsymbol{z}(t) \|$. Therefore, $\boldsymbol{e}(t)$ asymptotically converges to zero with time. □

Propositions 1 and 2 and the fact that (13) is globally invertible imply that the control aim in Eq. (8) is satisfied with the proposed controller (20).

4. Experimental Results

The experimental platform to evaluate the performance of the controllers integrates the Pioneer P3-DX mobile robot and *Optitrack* vision system as shown in Fig. 2. The vehicle pose is estimated with the vision system. An array of six cameras captures the movement of the robot, and the software *Motive-Optical motion capture* processes the images to obtain the position and orientation of the vehicle. The *Robot Operating System* (*ROS*) framework and *Simulink-Matlab* software were used to establish the wireless communication between the vision system and the robot. A program developed in *Simulink-Matlab* obtains the robot pose and computes the control law in terms of the linear and angular velocities, which are used as the control inputs. Finally, the *RosAria* node transforms the control velocities into voltages to drive the motors in the wheels. It is worthwhile to notice that although the Pioneer P3-DX is equipped with electrical motors as actuators, the actual control voltages are inaccessible. An internal controller converts the linear and angular velocity commands to voltage for the motors.

4.1. Performance of new scheme in simulation and experiment

In order to verify the effectiveness and the efficiency of the proposed controller, a simulation corresponding to the tracing of a circular path incorporating the effects of practical disturbances has been

https://doi.org/10.1017/S0263574718001443 Published online by Cambridge University Press

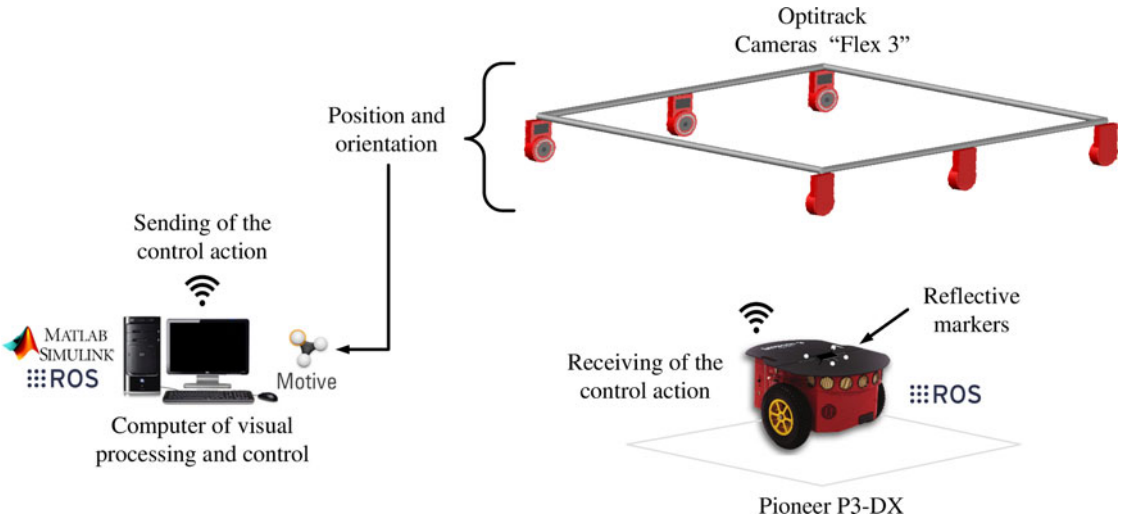


Fig. 2. Diagram of the experimental platform configuration for the Pioneer P3-DX mobile robot control.

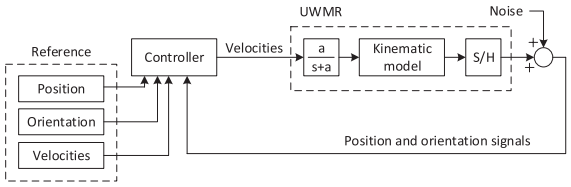


Fig. 3. Block diagram illustrating the considerations taken into account in the numerical simulation.

performed in *Simulink-Matlab*. The controller was programmed as discrete system with sampling time of 100 [ms]. The diagram of the simulation carried out is shown in Fig. 3. The blocks are described as follows:

- **Controller**: This block corresponds to the control law described by Eqs. (28) and (29).
- **Low pass filter:** This block is represented in the Laplace domain as $\frac{a}{s+a}$, which has the purpose of modeling the delay produce by the robot actuators. We have select $a = 20\pi$ [rad/s].
- **Kinematic model:** This block represents the model given in the Eqs. (1)–(3).
- **S/H:** This block represents the sampling and hold operation and is used to take samples of the output signals of the kinematic model at a constant rate of 100 [ms].

Besides, white noise is added to the translational and angular signals in order to simulate the noise produced by the vision system.

The circular reference path used for the simulation is defined by the following desired position and orientation:

$$x_r(t) = 0.5\sin(0.4t)\ [\text{m}], \tag{38}$$
$$y_r(t) = 0.5 - 0.5\cos(0.4t)\ [\text{m}], \tag{39}$$
$$\theta_r(t) = 0.4t\ [\text{rad}], \tag{40}$$

where $x_r(t)$ and $y_r(t)$ are the desired position of the robot in the plane. It is easy to prove that Eqs. (38)–(40) satisfy the virtual reference UWMR in Eqs. (5)–(7).

By using the Eqs. (10) and (11), and after obtaining the first and second time derivatives of the desired position, the linear and angular velocities yield

$$V_r = 0.2\ [\text{m/s}], \tag{41}$$
$$W_r = 0.4\ [\text{rad/s}]. \tag{42}$$

https://doi.org/10.1017/S0263574718001443 Published online by Cambridge University Press

Table I. **Circular path:** gains selected for each controller.

DDZB	**CKSS**	**PLLN**	**New Controller**	
$k_1 = 0.50$	$\alpha = 1.000$	$c_1 = 0.4$	$\alpha_1 = 0.7$	$\beta_1 = 0.05$
$k_2 = 0.16$	$\zeta = 0.075$	$c_2 = 1.0$	$\alpha_2 = -0.8$	$\beta_2 = -0.57$
			$\alpha_3 = 0.0$	$\beta_3 = 0.02$
			$k_{p1} = 0.4$	$k_0 = 2.0$
			$k_{p2} = 0.394$	

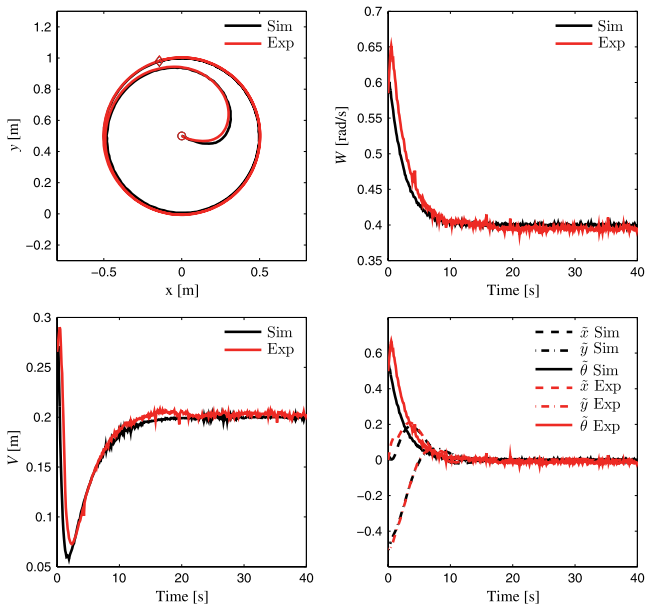


Fig. 4. **Novel controller:** comparison of the simulation result (black line) and the experimental (red line) result.

The initial configuration of the mobile robot for the numerical simulation with the circular path is as follows:

$$x_c(0) = \ \ 0.00 \text{ [m]}, \tag{43}$$
$$y_c(0) = \ \ 0.50 \text{ [m]}, \tag{44}$$
$$\theta(0) = -0.50 \text{ [rad]}. \tag{45}$$

The gains selected for the proposed controller fulfill the conditions given in Eqs. (24), (25), (26), and (35). The gains are shown in the column named "New controller" in Table I.

A real-time experiment was carried out using the same trajectory reference, the initial conditions, and gains as described for the simulation.

The results obtained in simulation and experiment are shown in Fig. 4. It is possible to observe small differences in the obtained numerical and experimental results. However, differences between simulation and experiment can be attributed to effects such as friction, wheel slipping, and communication delays, which were not taken into account in the numerical simulation.

To compare the performance of the controller, the root mean square (RMS) values of $\tilde{x}(t)$, $\tilde{y}(t)$, $\tilde{\theta}(t)$, $V(t)$, and $W(t)$ were computed in the time interval 20 [s] $\leq t \leq$ 40 [s], where transients are considered vanished. Table II presents the RMS values obtained in numerical simulation and real-time experiment.

4.2. Controllers for comparison

In this subsection, the selected controllers for the performance comparison are described. Different control techniques have been implemented to test the performance of the proposed scheme, which was described in Section 3.

https://doi.org/10.1017/S0263574718001443 Published online by Cambridge University Press

Table II. **Novel controller:** RMS values in numerical simulation and real-time experiment.

	20 [s] ≤ t ≤ 40 [s]				
RMS	$\tilde{x}$ **[m]**	$\tilde{y}$ **[m]**	$\tilde{\theta}$ **[rad]**	V **[m/s]**	W **[rad/s]**
Simulation	0.0012	0.0010	0.0031	0.1998	0.4000
Experiment	0.0030	0.0034	0.0147	0.2026	0.3949

4.2.1. Controller proposed by Dixon, Dawson, Zergeroglu, and Behal[20]. The controller reported by Dixon *et al.*,[20] which was developed using techniques such as that of Lyapunov, is given by

$$\begin{bmatrix} V \\ W \end{bmatrix} = \begin{bmatrix} k_1 e_1 + V_r \cos(e_3) \\ V_r \frac{\sin(e3)}{e_3} e_2 + k_2 e_3 + W_r \end{bmatrix}, \tag{46}$$

where $k_1, k_2 \in \mathbb{R}$ are positive constants.

Because of its developers, the scheme (46) is denoted as the DDZB controller.

4.2.2. Controller proposed by Canudas de Wit, Khennouf, Samson, and Sordalen[21]. The controller reported by Canudas de Wit *et al.*,[21] which was developed using a linearized model, is given by

$$\begin{bmatrix} V \\ W \end{bmatrix} = \begin{bmatrix} V_r \cos(e_3) + k_1 e_1 \\ W_r + k_2 sign(V_r) e_2 + k_3 e_3 \end{bmatrix}, \tag{47}$$

with $k_1 = 2\zeta a$, $k_2 = \frac{a^2 - W_r^2}{|V_r|}$, and $k_3 = 2\zeta a$, where ζ and $a \in \mathbb{R}$ are positive constants. Similarly, the algorithm (47) is called the CKSS controller.

4.2.3. Controller proposed by Panteley, Lefeber, Loría, and Nijmeijer[22]. The controller reported by Panteley *et al.*[22] has the following cascade structure:

$$\begin{bmatrix} V \\ W \end{bmatrix} = \begin{bmatrix} V_r + c_2 e_1 \\ W_r + c_1 e_3 \end{bmatrix}, \tag{48}$$

where c_1 and $c_2 \in \mathbb{R}$ are positive constants. The controller (48) is denoted as the PLLN scheme because of its developers.

4.3. Experimental comparison by using a circular path

For this set of experimental comparisons, the circular path in Eqs. (38)–(40) has been used. The reference linear and angular velocities are expressed in Eqs. (41) and (42). The initial configuration of the Pioneer P3-DX mobile robot for all experiments with the circular path is shown in Eqs. (43)–(45).

The gains for each controller were selected by a trial-and-error process such that there was no variation outside a range of ±5% of the RMS value of V and W of one controller with respect to the others in the time interval 20 [s] ≤ t ≤ 40 [s]. The obtained gains are shown in Table I.

The results of the real-time experiments are shown in Figs. 5–7. The green, blue, and yellow lines are associated with the controllers DDZB, CKSS, and PLLN, respectively, and the red lines correspond to the results from the scheme proposed in Eq. (20). The paths described using the four controllers are shown in Fig. 5. The left-hand side of Fig. 6 presents the time evolution of the robot pose $x_c(t)$, $y_c(t)$, and $\theta(t)$ in comparison to the desired values $x_r(t)$, $y_r(t)$, and $\theta_r(t)$. The pose error signals $\tilde{x}(t)$, $\tilde{y}(t)$, and $\tilde{\theta}(t)$ are also shown in the right-hand side of Fig. 6.

The time evolution of the control inputs $V(t)$ and $W(t)$ is presented in Fig. 7. The difference between the reference control inputs and the actual control inputs,

$$\tilde{V} = V_r - V, \tag{49}$$

$$\tilde{W} = W_r - W, \tag{50}$$

is also shown in Fig. 7.

Similar performances are observed for all controllers, with the main difference in the transient period.

https://doi.org/10.1017/S0263574718001443 Published online by Cambridge University Press

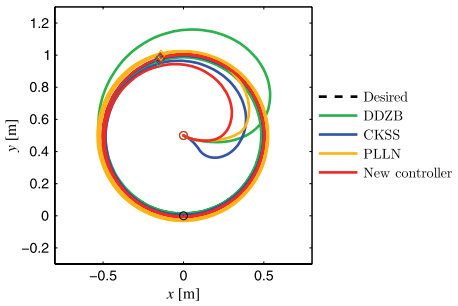


Fig. 5. **Experimental results:** paths drawn by the P3-DX mobile robot using the controllers DDZB (green line), CKSS (blue line), PLLN (yellow line), and the proposed scheme (red line). The starting point is depicted by (o, o, o and o), and the final position is depicted by ($\diamond$, $\diamond$, $\diamond$, and $\diamond$).

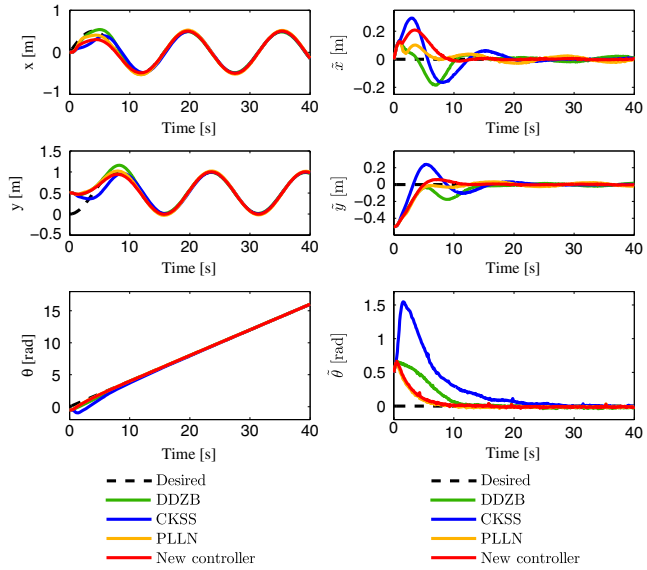


Fig. 6. **Experimental results:** (left) time evolution of $x(t)$, $y(t)$, and $\theta(t)$ obtained using the controllers DDZB (green line), CKSS (blue line), and PLLN (yellow line), and the proposed scheme (red line); (right) time evolution of the tracking error $\tilde{x}(t)$, $\tilde{y}(t)$, and $\tilde{\theta}(t)$ obtained using the four tested controllers.

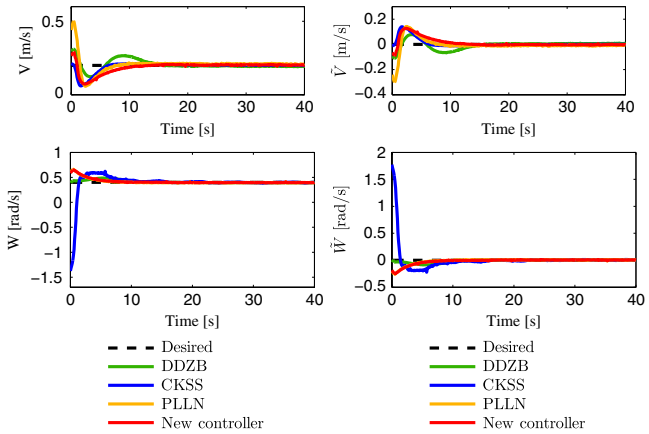


Fig. 7. **Experimental results:** (left) time evolution of the actual control inputs obtained using the controllers DDZB (green line), CKSS (blue line), and PLLN (yellow line), and the proposed scheme (red line); (right) control input errors obtained using the four tested controllers.

https://doi.org/10.1017/S0263574718001443 Published online by Cambridge University Press

Table III. **Experimental results for the circular path:** RMS values for comparison of the controllers DDZB (46), CKSS (47), and PLLN (48), and the proposed scheme (20).

	20 [s] ≤ t ≤ 40 [s]						
RMS	$\tilde{x}$ **[m]**	$\tilde{y}$ **[m]**	$\tilde{\theta}$ **[rad]**	$\tilde{V}$ **[m/s]**	$\tilde{W}$ **[rad/s]**	V **[m/s]**	W **[rad/s]**
DDZB	0.0130	0.0102	0.0228	0.0055	0.0060	0.1948	0.3942
CKSS	0.0076	0.0082	0.0232	0.0016	0.0077	0.2008	0.3980
PLLN	0.0167	0.0163	0.0149	0.0092	0.0060	0.2088	0.3946
New Controller	0.0030	0.0034	0.0147	0.0031	0.0057	0.2026	0.3949

Table IV. **Lemniscate path:** gains selected for each controller.

DDZB	**CKSS**	**PLLN**	**New Controller**	
$k_1 = 0.45$ $k_2 = 0.90$	$\alpha = 1.107$ $\zeta = 0.300$	$c_1 = 0.5$ $c_2 = 1.0$	$\alpha_1 = 0.9$ $\alpha_2 = -1.3 \times W_r(t)$ $\alpha_3 = 0.0$ $k_{p1} = 1.6$ $k_{p2} = 1.3$	$\beta_1 = 1.0$ $\beta_2 = -1.44 \times W_r(t)$ $\beta_3 = 10.0$ $k_0 = 1.3$

To compare the performance of the controllers, the RMS values of $\tilde{x}(t)$, $\tilde{y}(t)$, $\tilde{\theta}(t)$, $\tilde{V}(t)$, $\tilde{W}(t)$, $V(t)$, and $W(t)$ were computed in the time interval 20 [s] $\leq t \leq$ 40 [s], which is associated with the steady state. Table III presents the RMS values obtained with each controller. The proposed controller shows the best performance with the lowest RMS values for the pose error signals. In addition, the RMS values of the control inputs for all controllers do not differ by more than ±5%. Thus, with identical energy consumption, the new controller performs better.

4.4. Experimental comparison by using a lemniscate path

A lemniscate reference path was used to carried out another set of real-time experiments. This path is defined by the following reference position and orientation signals:

$$x_r(t) = 1.1 + 0.7 \sin\left(\frac{2\pi t}{30}\right)[\text{m}], \tag{51}$$

$$y_r(t) = 0.9 + 0.7 \sin\left(\frac{4\pi t}{30}\right)[\text{m}], \tag{52}$$

$$\theta_r(t) = \text{atan2}\,(\dot{y}_r, \dot{x}_r)\,[\text{rad}]. \tag{53}$$

The Eqs. (51)–(53) satisfy the virtual reference UWMR (5)–(7), which can be verified by direct algebra.

The reference linear velocity $V_r(t)$ and reference angular velocity $W_r(t)$ were computed by using the expressions (10) and (11), whose explicit description is omitted for shortening of this paper.

For this set of experiments, the initial configuration of the Pioneer P3-DX mobile robot is

$$x_c(0) = 1.2\ [\text{m}], \tag{54}$$

$$y_c(0) = 0.9\ [\text{m}], \tag{55}$$

$$\theta(0) = 0.7854\ [\text{rad}]. \tag{56}$$

As in the previous set of experiments, the gains for each controller were selected such that the difference of the RMS values of the input signals V and W fell within a range of variation ±5% of one controller with respect to the others. The obtained gain values are shown in Table IV. Besides, the gains of the proposed controller satisfy conditions (24), (25), (26), and (35).

The results of the real-time experiments are depicted in Figs. 8–10. The paths described using each controller are shown in Fig. 8. The time evolution of the robot state $x_c(t)$, $y_c(t)$, and $\theta(t)$ and their desired values $x_r(t)$, $y_r(t)$, and $\theta_r(t)$ are presented in Fig. 9. The error signals $\tilde{x}(t)$, $\tilde{y}(t)$, and $\tilde{\theta}(t)$ are also shown in Fig. 9. Fig. 10 shows the time evolution of control inputs $V(t)$ and $W(t)$ and the difference between the desired control input and the actual control input given in Eqs. (49) and (50).

https://doi.org/10.1017/S0263574718001443 Published online by Cambridge University Press

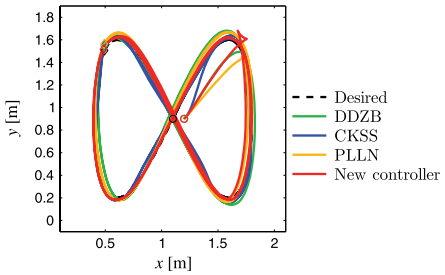


Fig. 8. **Experimental results:** paths drawn by the P3-DX mobile robot for the controllers DDZB (green line), CKSS (blue line), and PLLN (yellow line), and the proposed scheme (red line). The starting point is depicted by (o, o, o and o), and the final position is depicted by (◇, ◇, ◇, and ◇).

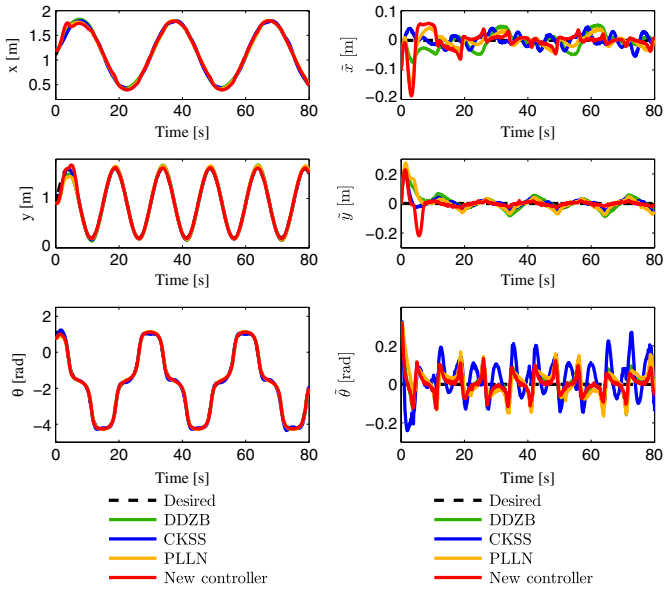


Fig. 9. **Experimental results:** (left) time evolution of $x(t)$, $y(t)$, and $\theta(t)$ obtained using the controllers DDZB (green line), CKSS (blue line), and PLLN (yellow line), and the proposed scheme (red line); (right) time evolution of the tracking error $\tilde{x}(t)$, $\tilde{y}(t)$, and $\tilde{\theta}(t)$ obtained using the four controllers.

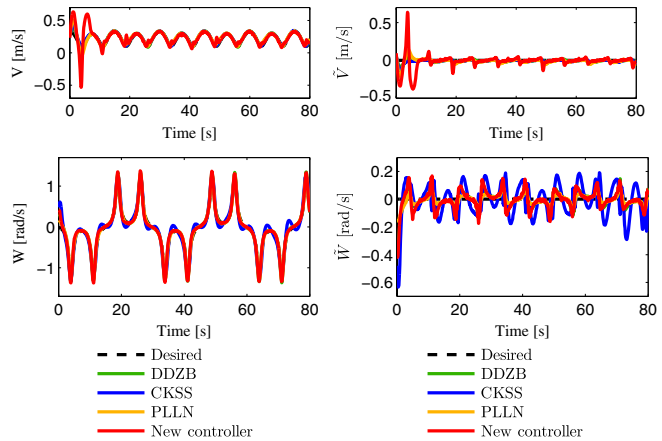


Fig. 10. **Experimental results:** (left) time evolution of the actual control inputs obtained using the controllers DDZB (green line), CKSS (blue line), and PLLN (yellow line), and the proposed scheme (red line); (right) control input errors obtained using the four controllers.

https://doi.org/10.1017/S0263574718001443 Published online by Cambridge University Press

Table V. **Experimental results for the lemniscate path:** RMS values for the comparison of the controllers DDZB (46), CKSS (47), and PLLN (48), and the proposed scheme (20).

	40[s]≤ t ≤ 80[s]						
RMS	$\tilde{x}$**[m]**	$\tilde{y}$**[m]**	$\tilde{\theta}$**[rad]**	$\tilde{V}$**[m/s]**	$\tilde{W}$**[rad/s]**	V**[m/s]**	W**[rad/s]**
DDZB	0.0237	0.0351	0.0605	0.0130	0.0553	0.2372	0.5601
CKSS	0.0205	0.0236	0.0993	0.0127	0.1120	0.2350	0.5625
PLLN	0.0192	0.0328	0.0653	0.0211	0.0327	0.2377	0.5509
New Controller	0.0132	0.0106	0.0425	0.0263	0.0552	0.2319	0.5570

Table VI. Percent improvement of the proposed controller with respect to controllers DDZB, CKSS, and PLLN, as computed from the RMS values for the implementations of the circular and lemniscate paths.

	DDZB		**CKSS**		**PLLN**	
Signal	**Circular path**	**Lemniscate path**	**Circular path**	**Lemniscate path**	**Circular path**	**Lemniscate path**
$\tilde{x}$	76.92%	44.3%	60.53%	35.61%	82.04%	31.25%
$\tilde{y}$	66.67%	69.8%	58.54%	55.08%	79.14%	67.68%
$\tilde{\theta}$	35.53%	29.75%	36.64%	57.2%	1.34%	34.92%
V	−4.00%	2.23%	−0.9%	1.32%	2.97%	2.44%
W	−0.18%	0.55%	0.78%	0.98%	−0.08%	−1.11%

To assess the performance of the tested controllers, the RMS values of the errors and control input signals were computed in the time interval 40 [s] $\leq t \leq$ 80 [s], where the transients vanished. Table V presents the results for the four controllers. The proposed controller shows the best performance with the lowest RMS values for the pose error signals. Similarly, the RMS values of the control inputs for all controllers do not differ by more than ±5%.

4.5. Discussions

In both sets of experiments, the introduced feedback linearization controller shows the best tracking accuracy under identical energy consumption as the other controllers. To complement the experimental study, Table VI shows the percent improvement of the proposed controller with respect to the controllers DDZB, CKSS, and PLLN, which was computed from the RMS values of the trajectory tracking error and control action for the implementations of the circular and lemniscate paths. The tracking errors are always improved with the proposed scheme. In addition, the relative improvement of the RMS values of the control actions V and W is always in the range of ±5%, as established in the gain tuning criterion.

The proposed controller has square terms in the tracking errors e_1, e_2, and e_3, as demonstrated by expanding Eqs. (28) and (29), which makes it a locally high-gain controller. This characteristic improves the attenuation of the effects of slowly varying disturbances, such as communication delays and friction, present in the experimental system.

5. Conclusions

A new controller based on the output feedback linearization design technique was introduced. A stability analysis of the closed-loop system was presented, and the local asymptotic stability was proven. The proposed controller was tested in numerical simulation and compared with experimental result under the same conditions. Besides, known schemes in the literature were compared to the proposed approach experimentally. Comparisons were made by using real-time experiments where two different motion tasks were specified. The Pioneer P3-DX UWMR and Optitrack vision system were used to perform real-time experiments. Finally, the experimental results show that the new controller provides the best tracking under identical energy consumption.

Further research consists of developing velocity-based control schemes[31,32] to achieve the motion control of UWMRs.

https://doi.org/10.1017/S0263574718001443 Published online by Cambridge University Press

Acknowledgments
This work was supported by CONACYT Project A1-S-24762 and Cátedras 1537, México.

References

1. J. Moreno–Valenzuela and C. Aguilar–Avelar, *Motion Control of Underactuated Mechanical Systems*, 1st ed. (Springer International Publishing AG, Cham, 2018).
2. C. Chevallereau, A. Formal'sky and D. Djoudi, "Tracking a joint path for the walk of an underactuated biped," *Robotica*. **22**(1), 15–28 (2004).
3. A. Zhang, C. Yang, S. Gong and J. Qiu, "Nonlinear stabilizing control of underactuated inertia wheel pendulum based on coordinate transformation and time-reverse strategy," *Nonlinear Dyn*. **84**(4), 2467–2476 (2016).
4. G. V. Raffo, M. G. Ortega, V. Madero and F. R. Rubio, "Two-wheeled self-balanced pendulum workspace improvement via underactuated robust nonlinear control," *Control Eng. Pract*. **44**, 231–242 (2015).
5. C. Han, J. Guo and A. Pechev, "Nonlinear H_∞ based underactuated attitude control for small satellites with two reaction wheels," *Acta Astronaut*. **104**(1), 159–172 (2014).
6. M. A. M. Basari, A. R. Husain and K. A. Danapalasingam, "Stabilization and trajectory tracking control for underactuated quadrotor helicopter subject to wind-gust disturbance," *Sadhana*. **40**(5), 1531–1553 (2015).
7. Z. Yan, H. Yu, W. Zhang, B. Li and J. Zhou, "Globally finite-time stable tracking control of underactuated UUVs," *Ocean Eng*. **107**, 132–146 (2015).
8. T. Elmokadem, M. Zribi and K. Youcef-Toumi, "Trajectory tracking sliding mode control of underactuated AUVs," *Nonlinear Dyn*. **84**(2), 1079–1091 (2016).
9. D. Diaz and R. Kelly, "On Modeling and Position Tracking Control of the Generalized Differential Driven Wheeled Mobile Robot," *Proceedings of the IEEE International Conference on Automatica (ICA–ACCA)*, Curico (2016) pp. 1–6.
10. X. Zhang , Y. Fang and N. Sun, "Visual servoing of mobile robots for posture stabilization: From theory to experiments," *Int. J. Robust Nonlin*. **25**(1), 1–15 (2014).
11. Y. Wang, Z. Miao, H. Zhong and Q. Pan, "Simultaneous stabilization and tracking of nonholonomic mobile robots: A Lyapunov-based approach," *IEEE Trans. Control Syst. Technol*. **23**(4), 1440–1450 (2015).
12. X. Chen and Y. Jia, "Simple tracking controller for unicycle-type mobile robots with velocity and torque constraints," *Trans. Inst. Meas. Control*. **37**(2), 211–218 (2014).
13. S. Millan and F. Valenciaga, "A Comparative Study of Two Trajectory Tracking Controllers for an Autonomous Robot Vehicle," *Proceedings of XVI Workshop on Information Processing and Control (RPIC)*, Córdoba (2015) pp. 1–6.
14. X. Li, Z. Wang, X. Chen, J. Zhu and Q. Chen, "Adaptive Control of Unicycle-type Mobile Robots with Longitudinal Slippage," *Proceedings of American Control Conference (ACC)*, Boston (2016) pp. 1637–1642.
15. S. Blažič, "Two Approaches for Nonlinear Control of Wheeled Mobile Robots," *Proceedings of the IEEE 13th International Conference on Control & Automation (ICCA)*, Ohrid (2017) pp. 946–951.
16. M. H. Korayem, R. A. Esfeden and S. R. Nekoo, "Path planning algorithm in wheeled mobile manipulators based on motion of arms," *J. Mech. Sci. Technol*. **29**(4), 1753–1763 (2015).
17. M. H. Korayem, M. Yousefzadeh and S. Manteghi, "Dynamics and input-output feedback linearization control of a wheeled mobile cable-driven parallel robot," *Multibody Syst. Dyn*. **40**(1), 55–73 (2017).
18. R. Liu, X. Sun and D. Wang, "Heavyweight airdrop flight control design using feedback linearization and adaptive sliding mode," *Trans. Inst. Meas. Control*. **38**(10), 1155–1164 (2016).
19. A. Mahmood and Y. Kim, "Decentrailized formation flight control of quadcopters using robust feedback linearization," *J. Franklin Inst*. **354**(2), 852–871 (2017).
20. W. Dixon, D. Dawson, E. Zergeroglu and A.Behal, *Nonlinear Control of Wheeled Mobile Robots*, 1st ed. (Springer-Verlag, London, 2001).
21. C. Canudas de Wit, H. Khennouf, C. Samson and O. J. Sordalen, "Nonlinear Control Design for Mobile Robots," **In**: *Recent Trends in Mobile Robots* (Y. F. Zheng, Ed.) (World Scientific Publishing, Singapore, 1993) pp. 121–156.
22. E. Panteley, E. Lefeber, A. Loria and H. Nijmeijer, "Exponential tracking control of a mobile car using a cascaded approach," *IFAC Proc. Vol.* **31**(27), 201–206 (1998).
23. I. Fantoni and R. Lozano, *Non–Linear Control for Underactuated Mechanical Systems*, 1st ed. (Springer-Verlag, London, 2002).
24. I. Anvari, Non-holonomic Differential Drive Mobile Robot Control & Design: Critical Dynamics and Coupling Constraints *M.Sc. Thesis* (Arizona State University, Tempe, USA, 2013).
25. M. Egerstedt, Motion Planning and Control of Mobile Robots *Ph.D. Thesis* (Royal Institute of Technology, Stockholm, Sweden, 2000).
26. T. Nascimento, C. DÃşrea and L. Gonçalves, "Nonholonomic mobile robots' trajectory tracking model predictive control: A survey," *Robotica*. **36**(5), 1–21 (2018).
27. H. K. Khalil, *Nonlinear Systems*, 3rd ed. (Prentice–Hall, Upper Saddle River, 2002).
28. J. J. E. Slotine and W. Li, *Applied Nonlinear Control*, 1st ed. (Prentice–Hall, Englewood-Cliffs, NJ, 1991).

https://doi.org/10.1017/S0263574718001443 Published online by Cambridge University Press

29. S. Sastry and M. Bodson, *Adaptive Control: Stability, Convergence, and Robustness*, 1st ed. (Prentice–Hall, Englewood-Cliffs, NJ, 1989).
30. E. Panteley and A. Loria, "On global uniform asymptotic stability of nonlinear time-varying systems in cascade," *Syst. Control Lett*. **33**(2), 131–138 (1998).
31. J. Moreno-Valenzuela, "Adaptive anti control of chaos for robot manipulators with experimental evaluations," *Commun. Nonlinear Sci. Numer. Simul*. **18**(1), 1–11 (2013).
32. J. Moreno-Valenzuela, "Velocity field control of robot manipulators by using only position measurements," *J. Franklin Inst*. **344**(8), 1021–1038 (2007).

https://doi.org/10.1017/S0263574718001443 Published online by Cambridge University Press